Polarization-Reconfigurable Yagi-Configured Electrically Small Antenna

Ming-Chun Tang, Qingli Lin, Mei Li, and Richard W. Ziolkowski

***Abstract*—An electrically small, high-directivity, Yagi-configured, near-field resonant parasitic (NFRP) antenna with four reconfigurable polarization states is presented. The antenna is composed of two NFRP elements and a customized, electrically-controlled, reconfigurable driven element. The elements are stacked vertically in a Yagi configuration. The upper NFRP element acts as the director, and the lower one acts as the reflector. Both elements have a cross-shaped Egyptian axe dipole form. By integrating four p-i-n (PIN) diodes into its coax-fed asymmetric driven element, four polarization states, i.e., two orthogonal linear polarization (LP) and two circular polarization (LHCP and RHCP), are enabled that are controlled with the ON/OFF states of the PIN diodes. The measured and simulated results of this electrically small (*ka* = 0.7) sized polarization-reconfigurable system are in good agreement. This simple, Yagi-configured antenna exhibits stable radiation performance in all four of its polarization states. The measured results demonstrate that in its *x (y)*-LP state, the peak realized gain, front-to-back ratio, and radiation efficiency values are, respectively, ~3.08 (3.2) dBi, ~11.0 (11.05) dB, and ~77% (73%), and that in its LHCP (RHCP) state they are, respectively, ~3.0 (3.1) dBi, ~ 12.1 (11.18) dB, and ~ 72% (70%).**

***Index Terms*—Electrically small antennas, near-field resonant parasitic elements, polarization-reconfigurable antennas, Yagi-configured antennas.**

I. Introduction

The Yagi-Uda antenna, which was invented by Yagi and Uda in 1928 [1], is a known end-fire radiating array with attractive features. It has a simple configuration that is low in cost to realize and yields a high directivity [2], [3]. Since then, different kinds of Yagi and quasi-Yagi arrays have been developed for many engineering applications, e.g., mobile vehicle-to-satellite systems [4], [5], high data-rate communication systems [6], point-to-point communication links [7], base stations [8], and commercial wireless local area networks (LANs) [9]-[11]. On the other hand, to achieve its higher directivity, a Yagi array is not electrically small, being long in its length. With the explosive development of wireless communication systems, the mobile platforms are becoming more compact and smarter. As a consequence, the room available for a long antenna system on them is becoming quite limited.

Several types of Yagi-configured electrically small antennas (ESAs) have been introduced to accommodate these space-limited platforms. These include systems combining spiral [12]，square-shaped [13], or crossed-dipole [14] drivers and directors, employing meander-line slotted coplanar waveguides (CPWs) [15], resorting to high-density electrically small dipole array concepts [16], [17], and utilizing two near-field resonant parasitic (NFRP) elements [18]. All of these approaches realized an enhanced directivity through some Yagi or quasi-Yagi type of reflector-driver-director configuration.

On the other hand, polarization-reconfigurable antennas hold many admirable advantages for compact wireless systems, e.g., they reduce the power loss, enhance anti-interference abilities, improve transmission efficiencies, and increase the system capacity [19], [20]. Many polarization-reconfigurable antennas have been reported, e.g., patch antennas [21]-[26]; filtennas [27], [28]; and substrate integrated waveguide (SIW) antennas [29], [30]. While they have been studied extensively, only a few polarization-reconfigurable Yagi-based systems have been investigated. Integrating polarization reconfigurability with a Yagi-configured ESA could provide many advantages for space-limited wireless applications.

A polarization-reconfigurable, Yagi-configured ESA with quad-polarization diversity is presented in this Communications paper. Because it is in a Yagi array configuration, the antenna will be described as an end-fire system even though the fields are radiated in the broadside direction from the elements. The antenna is composed of a NFRP-based director and a NFRP-based reflector, both of which are in the form of a pair of cross-shaped Egyptian axe dipoles (EADs), and a specially-engineered electrically-controlled driven element. The polarization reconfigurability is realized by integrating four PIN diodes into the driven element. By controlling their ON/OFF states, the induced current pathways on the NFRP elements are controlled to achieve four different polarization states, i.e., two linearly polarized (LP) states and two circularly polarized (CP) states. Because of the inherent rotational symmetry of the orthogonally-arranged NFRP director and reflector elements, there is no need to reconfigure them. The electrically small size of the overall system, $ka = 0.7$, with its four polarization diverse states and excellent end-fire radiation performance characteristics makes it a very attractive candidate for applications in space-limited wireless applications.

The antenna configuration and its operating mechanisms are explained in detail in Section II. A prototype of the optimized design was fabricated, assembled, and tested. As described in Section III, the measured performance characteristics are in good agreement with their simulated values, confirming the efficacy of this reconfigurable Yagi-based design. Finally, some conclusions are discussed in Section IV.

II. Antenna Design

A. Polarization-Reconfigurable ESA Configuration

Fig. 1 illustrates the configuration of the developed polarization-reconfigurable Yagi-configured ESA. As shown in Figs. 1(a) and (d), the antenna consists of three substrate layers. They are labeled as Layer_1, Layer_2 and Layer_3, respectively. All three substrates are Rogers 6010 with relative dielectric constant $\varepsilon_r = 10.2$, loss tangent $\tan\delta = 0.0023$, and copper cladding thickness 0.018 mm. All three layers have the same radius, R1 = 32.0 mm, and the same thickness, H1=1.27 mm. As is shown in Fig. 1(a), one metallic NFRP

Manuscript received on 29th, November, 2019; revised on 10th, June, 2020; and accepted on 4th, August, 2020. This work was supported in part by the National Natural Science Foundation of China contract number 61922018, in part by the Funding of the leading research talent cultivation plan of Chongqing University contract number cqu2017hbrc1A08, in part by the Funding of the Innovative Leading Talents in Science and Technology of Chongqing contract number CSTCCXLJRC201705, in part by the Chongqing Natural Science Foundation contract number cstc2019jcyjjqX0004, and in part by the Australian Research Council grant number DP160102219.

M. -C. Tang, Q. Lin, and M. Li are with the Key Laboratory of Dependable Service Computing in Cyber Physical Society Ministry of Education, School of Microelectronics and Communication Engineering, Chongqing University, Chongqing 400044, China (e-mail: tangmingchun@cqu.edu.cn);

R. W. Ziolkowski is with the University of Technology Sydney, Global Big Data Technologies Centre, Ultimo NSW 2007, Australia (e-mail: richard.ziolkowski@uts.edu.au).

element in the form of cross-EADs is printed on the upper surface of Layer_1, which acts as the director. The middle layer, Layer_2, supports the driven element, which is printed on its lower surface. It has a crossed-dipole form in which one end of each dipole is terminated with a top-hat curved arc. Four PIN-diodes are integrated into the driven element. Its center two pieces are connected to the 50-Ω coaxial feed line through two parallel vertical strips. The bottom layer, Layer_3, has another cross-EAD NFRP element printed on its upper surface, which acts as the reflector.

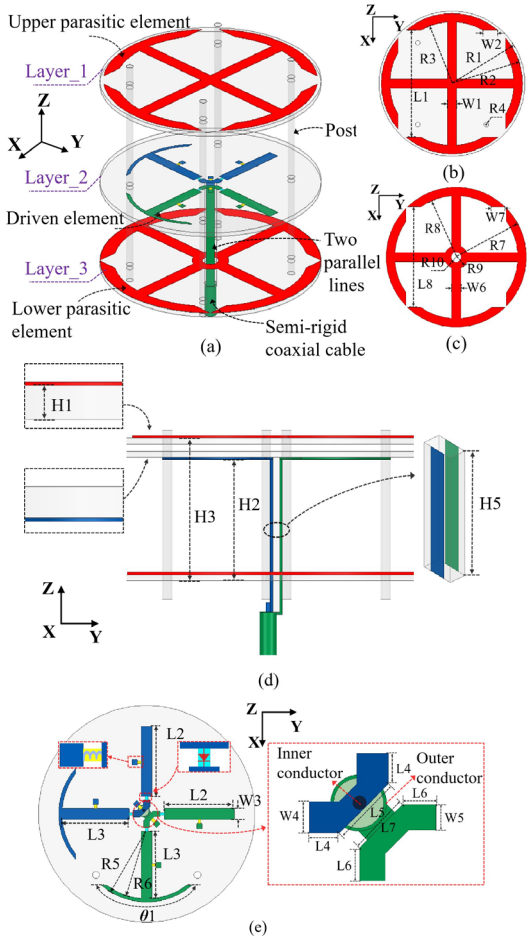

Fig. 1 Configuration and design parameters of the polarization-reconfigurable Yagi-configured ESA. (a) 3-D isometric view. Upper surfaces of (b) Layer_1 and (c) Layer_3. (d) Side view. (e) Lower surface of Layer_2.

The configurations of the upper and lower NFRP elements are depicted and their design parameters are given in Figs. 1(b) and (c), respectively. It is shown that the two NFRP elements are both in the form of cross-shaped EADs. A hole with a radius, R10, is drilled through the center of the lower NFRP element to allow the driven-element feed to pass through it without shorting. Notice that, the dimensions of the two cross-shaped EADs are different; the director has a radius smaller than the reflector's radius, which coincides with the radius of Layer_3.

The driven element is differentially-fed by those two parallel strips. One is connected to the center conductor of the coax; the other is connected to its outer conductor, as is shown in Fig. 1(d). These parallel lines are printed on a Rogers 4350 substrate with a relative dielectric constant of 3.48 and a thickness of 1.524 mm. The length and width of the parallel lines are H5 and W7, respectively.

There are air gaps between the three layers. In order to ensure the mechanical stability of the structure, the height of each layer was fixed by four hexagonal plastic screws and 24 (2 per layer, 6 per screw) plastic nuts. Four holes were drilled symmetrically with respect to the *x*- and *y*- axes through each substrate. Each hole has a radius, R4, which is large enough for the long plastic screws to pass through each dielectric layer. The plastic screws and nuts do not affect the radiation performance of the antenna. The spacing between the director and the driven element, H3-H2, significantly impacts the capacitive coupling level between the director and the driven element. According to the NFRP ESA design methodology [16], this feature provides a means to finely tune the resonance frequency and the impedance match to the source. On the other hand, as was reported in [31], the spacing between the director and the reflector, H3, should be on the order of 0.1 λ_0 and their phase difference should be ~180° over the entire operational frequency range to realize relatively stable end-fire radiation characteristics.

The design parameters of the driven element are detailed in Fig. 1(e). As noted above, it consists of two cross-shaped top-hat-loaded dipoles. The integrated PIN diodes divide this structure into four disconnected segments. One end of each PIN diode is soldered to the inner end of one segment and the other end is electrically connected to the conducting pieces attached to the inner and outer conductors of the coax. This configuration allows for the independent control of the ON/OFF state of all four PIN diodes and, hence, of the current pathways from the feed to the different segments. The addition of the two curved top-hats contributes the driven element's asymmetry along the *x*- and *y*-axis and is a configuration quite different from our previous designs [16], [17], [18]. This specially-engineered structure provides the means to achieve the requisite 90° phase difference when the system operates in its LHCP or RHCP state.

The final, optimized design parameters are detailed in Table I.

TABLE I
OPTIMIZED DESIGN PARAMETERS OF THE POLARIZATION-RECONFIGURABLE ESA (DIMENSIONS IN MILLIMETERS)

R1=32	*R2=31*	*R3=27.3*	*R4=1.05*	*R5=20.5*
R6=19.5	*R7=31.9*	*R8=28*	*R9=5.32*	*R10=2.32*
L1=47.2	*L2=24.3*	*L3=24*	*L4=1.89*	*L5=4.4*
L6=2	*L7=3.85*	*L8=45.4*	*W1=3.9*	*W2=6.37*
W3=3.2	*W4=2*	*W5=1.6*	*W6=4*	*W7=2.4*
W8=3.5	*θ1=60°*	*H1=1.27*	*H2=26.27*	*H3=30.41*
H4=0.018	*H5=33*	*Null*		

B. Implementation of the Reconfigurable Driver

The detailed states of the four PIN diodes that realize each of the polarization states of the ESA and the corresponding current paths on the segments of the driven element are illustrated in Fig. 2. The orientations of the four PIN diodes, i.e., PIN_1, PIN_2, PIN_3 and PIN_4, are shown in Fig. 2. The relationships between those PIN diodes and polarization states are summarized in Table II. Each PIN diode is a surface mount M/A-COM BAR5002VH6327XTSA1 from Infineon Technologies. According to its datasheet, it acts as a 1.2 Ω resistor in its ON state and as a 0.015 pF capacitor in its OFF state [32].The ON/OFF state of each PIN diode is controlled through bias lines connected to a DC power supply. Square metallic pads (6) are printed next to the different segments of the driven element to provide attachment points for 6 RF current-block inductors. These inductors prevent any RF signals from entering the DC bias network and affecting the performance of the system. Each inductor is a SC79 package from Murata Electronics [33] and has an inductance of 100 nH.

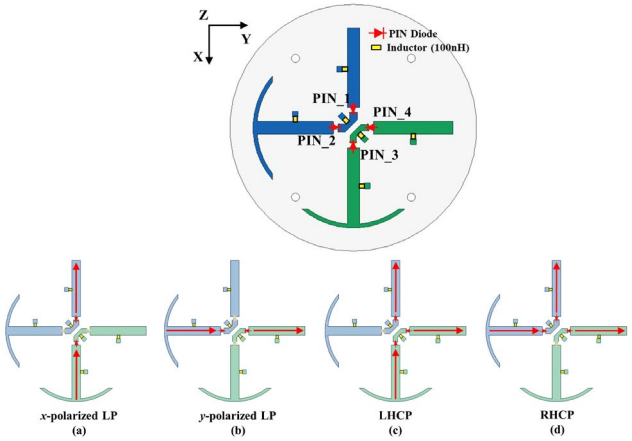

Fig. 2 The locations of the PIN diodes and inductors on the driven element are indicated in the top subplot. The current pathways on the driven element for different polarization states are shown in the bottom subplot. (a) *x*-polarized LP. (b) *y*-polarized LP. (c) LHCP. (d) RHCP.

TABLE II
THE PIN DIODE STATES TO ATTAIN THE FOUR POLARIZATION STATES

Category	*State*	*PIN_1*	*PIN_2*	*PIN_3*	*PIN_4*
Fig. 2 (a)	*x-LP*	*ON*	*OFF*	*ON*	*OFF*
Fig. 2 (b)	*y-LP*	*OFF*	*ON*	*OFF*	*ON*
Fig. 2 (c)	*LHCP*	*ON*	*OFF*	*ON*	*ON*
Fig. 2 (d)	*RHCP*	*ON*	*ON*	*OFF*	*ON*

The current pathway on the driven element for each polarization state is shown in Figs. 2(a)-(d). For the *x*-LP state, PIN_1 and PIN_3 operate in the ON state and PIN_2 and PIN_4 operate in the OFF state. The corresponding current pathway is shown in Fig. 2(a). Otherwise, the antenna operates in the *y*-LP state; the corresponding current pathway is shown in Fig. 2(b). For the LHCP state, PIN_2 operates in the OFF state and others operate in the ON state. The corresponding current pathway is shown in Fig. 2(c). In contrast, PIN_3 operates in the OFF state and others operate in the ON state for the RHCP state. The corresponding current pathway is shown in Fig. 2(d).

The operating mechanisms of the polarization-reconfigurable ESA can be explained by the director-driver-reflector Yagi configuration and its principles. This explanation is facilitated by examining the surface current distributions on the upper (director) and lower (reflector) NFRP elements and the driven element over one period. They are shown in Figs. 3 and 4 at the same frequency, 0.95 GHz, which is a frequency point located in all four operational bands. Since the operating principles of both LP (CP) states are essentially the same, only the *x*-LP and the LHCP states are discussed.

For ease of understanding, the current directions are highlighted with the additional colored arrows in Figs. 3 and 4. The currents on the two NFRP elements shown in Fig. 3 are uniformly distributed along the *x*-axis direction throughout the entire period. This illustrates that only currents on the EAD segments oriented along the *x*-axis are strongly excited and, hence, yield the *x*-LP behavior. This outcome was expected because PIN_2 and PIN_4 are turned OFF so only minor currents are driven and, as a consequence, are induced along the *y*-axis.

Similarly, the current distributions for the LHCP state are depicted in Fig. 4. Because of its CP behavior, a more complicated set of colored arrows are provided with the red (blue) ones referring to the upper (lower) NFRP element. The currents distributed on both the upper and lower NFRP elements clearly rotate clockwise along a circle as the phase increases and, hence, they generate the LHCP field. The physical configuration of the ESA in this state has PIN_2 OFF and all of the other diodes ON. This configuration yields an asymmetric distribution of currents on the driven element in which the *x*-oriented segment with the top-hat is combined with the simple *y*-oriented one. Note that because they are in a very symmetric configuration, there are two orthogonal degenerate modes polarized in the *x*- and *y*-directions for the two NFRP elements. The asymmetric configuration on the driven element separates these two degenerate modes with a 90° phase difference, which leads to the LHCP radiation.

Moreover, as noted above, the spacing between the two NFRP elements is ~ 0.1 λ_0 and their phase difference is ~ 180° over the entire frequency range to realize relatively stable end-fire radiation characteristics. This phase difference phenomenon, as expected from the theory presented in [31], [34], is also confirmed in Figs. 3 and 4.

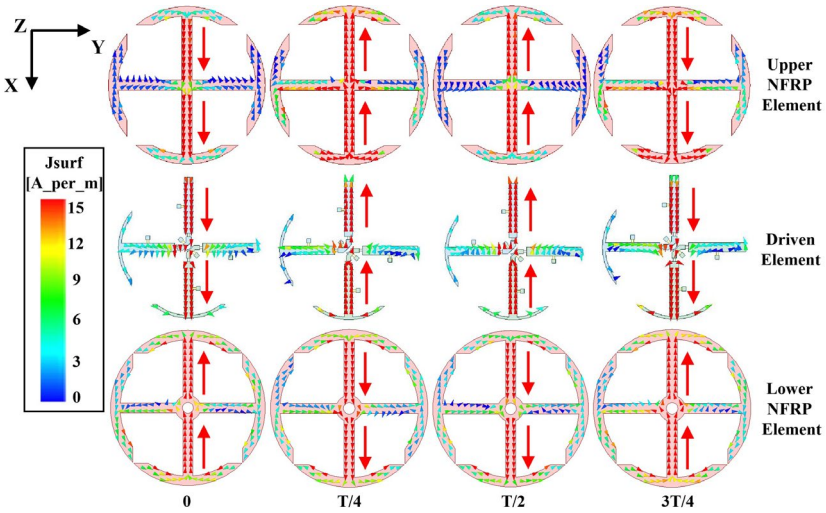

Fig. 3 Surface current distributions on the driven and upper and lower NFRP elements for the *x*-LP state at 0.95 GHz over one period.

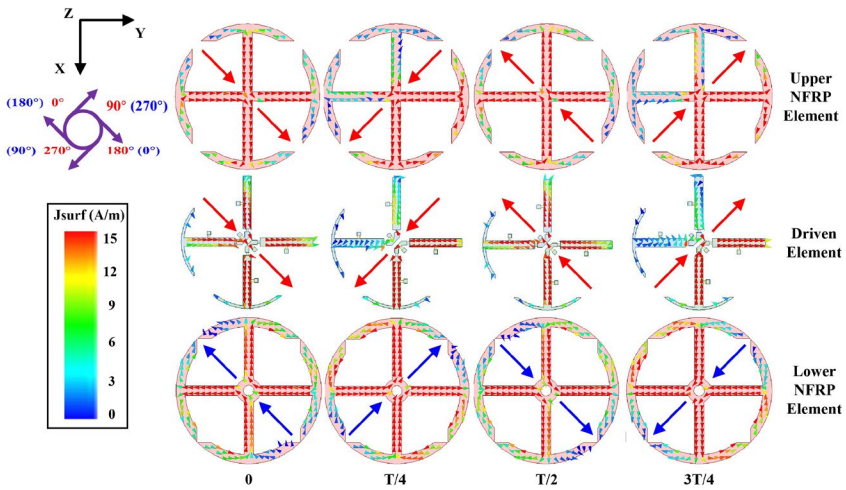

Fig. 4 Surface current distributions on the driven and upper and lower NFRP elements for the LHCP state operating at 0.95 GHz over one period.

III. Simulated and Measured Results

The optimized polarization-reconfigurable Yagi-configured ESA shown in Fig. 1 was fabricated, assembled, and measured. The fabricated layers and the assembled prototype are shown in Figs. 5(a) and 5(b), respectively. The reflection coefficient was measured with an Agilent Technologies E5071C network analyzer and the far-field characteristics of the prototype were measured in the multi-probe spherical near field test anechoic chamber shown in Fig. 5(c). The realized gain values, radiation patterns, and axial ratios (ARs), were obtained. Note that an ATTEN TPR3003T-3C regulated DC power supply was adopted for the biasing voltage in the measurements.

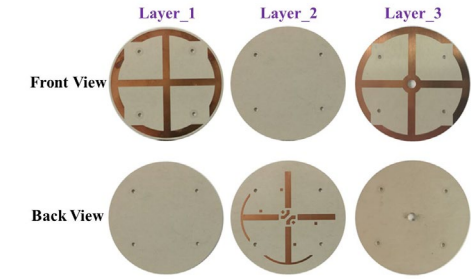

(a)

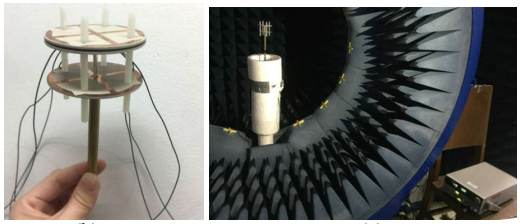

(b) (c)

Fig. 5 Fabricated polarization-reconfigurable ESA. (a) Front and back views of each layer before assembly. (b) 3-D isometric view. (c) Antenna under test (AUT) in the anechoic chamber.

The simulated and measured $|S_{11}|$ curves are shown in Fig. 6 for the *x*-LP, *y*-LP, LHCP, and RHCP states of the prototype. Fig. 6(a) indicates that the simulated –10-dB impedance bandwidths of the *x*- and *y*- LP states are, respectively, 4.7%, from 0.941 to 0.987 GHz (46 MHz) and 4.5%, from 0.942 to 0.986 GHz (44 MHz). The measured –10-dB impedance bandwidths of the *x*- and *y*- LP states are, respectively, 3.2% from 0.945 to 0.976 GHz (31 MHz) and 2.7% from 0.946 to 0.972 GHz (26 MHz). Therefore, the simulated (measured) overlapping operational bandwidth for the two LP states is 44 MHz (26 MHz), covering from 0.942 to 0.986 GHz (from 0.946 to 0.972 GHz).

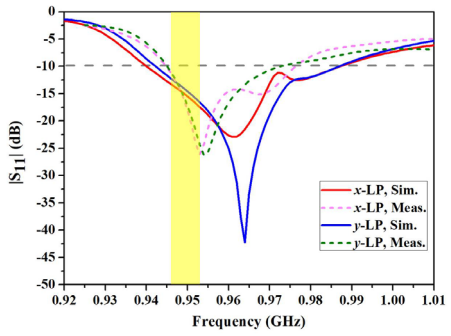

(a)

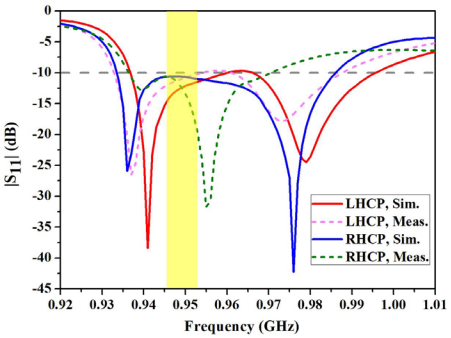

(b)

Fig. 6 Simulated and measured $|S_{11}|$ of the polarization-reconfigurable ESA. (a) Two LP states. (b) Two CP states. (The measured overlapping bandwidth is highlighted by the shadow region.)

Similarly Fig. 6(b) indicates that the simulated –10-dB impedance bandwidths of the LHCP and RHCP states are, respectively, 6.0% from 0.937 to 0.995 GHz (58 MHz) and 5.4% from 0.934 to 0.986 GHz (52 MHz). The measured –10-dB impedance bandwidths of the LHCP and RHCP states are, respectively, 5.4% from 0.934 t0 0.986 GHz (52 MHz) and 3.5% from 0.936 to 0.97 GHz (34 MHz). Consequently, the simulated (measured) overlapping impedance bandwidth for the two CP states is 49 MHz (34 MHz) covering from

0.937 to 0.986 GHz (from 0.936 to 0.97 GHz). Note that the differences between the simulated and measured $|S_{11}|$ values are quite acceptable. For instance, the measured *y*-LP resonance frequency, 0.964 GHz, in contrast to its simulated value, 0.953 GHz, is only a 1.1% difference. The observed discrepancies, as confirmed with simulations, arise from inevitable errors in the fabrication, assembly and experimental processes. For example, non-uniformity of the gaps between the three substrate layers occurs even though the plastic screws and nuts introduced for mechanical support should ensure their sameness. Furthermore, the long DC biasing lines present in the measurements are not taken into consideration in the simulations.

The far-field radiation performance was measured in an anechoic chamber at the National Key Laboratory of Science and Technology on Communications, University of Electronic Science and Technology of China (UESTC). This facility is based mainly on the Agilent N5230A PNA-L VNA and the SATIMO passive measurement system (0.8–6 GHz) [35]. It can directly measure the realized gain (RG), directivity, AR, radiation efficiency (RE), and other performance characteristic values.

The simulated and measured AR values of the two CP states are plotted in Fig. 7. The simulated 3-dB bandwidths of the LHCP and RHCP states are the same, 0.84% covering from 0.946 to 0.954 GHz (8 MHz). The measured AR values for the two CP states are in the range of 0.73% from 0.946 to 0.953 GHz (7 MHz). Considering both the –10-dB impedance and the 3-dB AR bandwidths, the measured overlapping operational bandwidth covered 7 MHz from 0.946 to 0.953 GHz for all four polarization reconfigurable states.

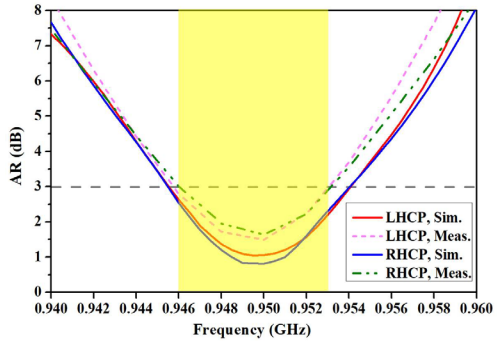

Fig. 7 Simulated and measured AR values of the polarization-reconfigurable ESA. (The measured overlapping bandwidth is highlighted by the shadow region.)

The simulated and measured normalized realized gain patterns of the *x*-LP, *y*-LP, LHCP, and RHCP states at the selected operational frequency, 0.95 GHz, which lies in the operational band of each polarization state, are plotted in Figs. 8 (a)-(d), respectively. One clearly sees that the antenna exhibits stable broadside radiation with good front-to-back ratio (FTBR) values, validating that it has excellent endfire radiation performance when it is viewed as a typical Yagi-configured system [1]. Good agreement between the simulated and measured values was clearly achieved. In particular, the simulated (measured) peak realized gain, FTBR, and RE values in the *x*-LP state are 3.8 (3.08) dBi, 10.93 (11.0) dB, and 87.9% (77%), respectively. The corresponding values in the *y*-LP state are 4.2 (3.2) dBi, 11.34 (11.05) dB, and 86% (73%), respectively. Moreover, the simulated and measured cross-polarization levels are both below –15 dB for the two LP states, indicating high polarization purity. The simulated (measured) peak realized gain, FTBR, and RE values in the LHCP state are 3.8 (3.0) dBi, 14.39 (12.1) dB, and 82% (72%), respectively. The corresponding values in the RHCP state are 3.8 (3.1)dBi, 14.72 (11.18) dB, and 82% (70%), respectively.

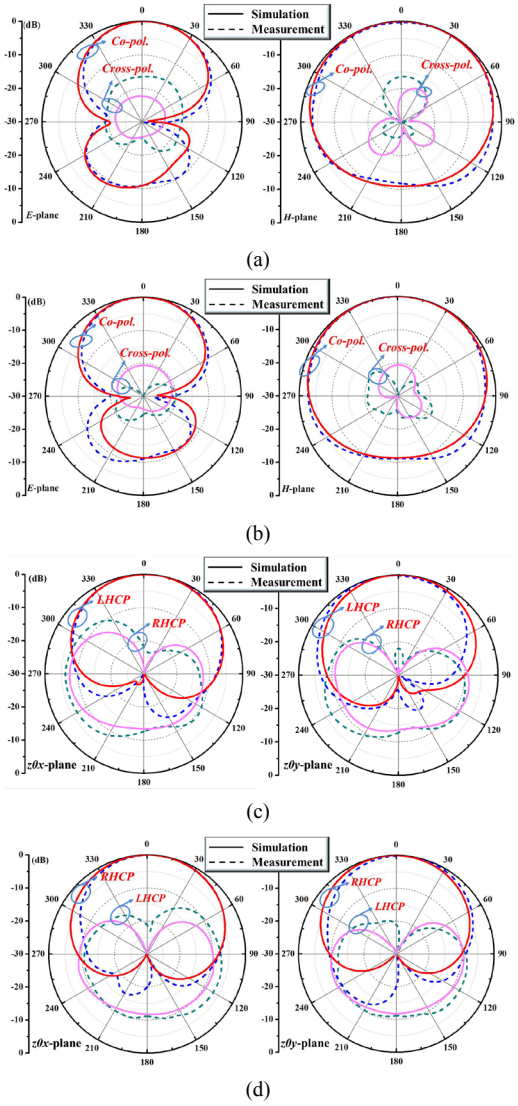

Fig. 8 The simulated and measured normalized realized gain patterns of the prototype operating at 0.95 GHz for all the four polarization states. (a) *x*-LP state. (b) *y*-LP state. (c) LHCP state. (d) RHCP state.

A performance comparison of the prototype polarization-reconfigurable ESA with recently reported related Yagi-configured ESAs is given in Table III. In contrast to the Yagi-configured ESAs in [12]-[18], the prototype realized four electronically switchable, polarization diverse states with an electrically small, ka = 0.7, system and high quality endfire radiation performance characteristics. The RG values in all four states of our prototype are not as high as those in [12]-[18]. This is simply due to two main reasons. First, our ESA was designed to simultaneously achieve essentially the same directional radiation and bandwidth performance in all four dynamic states. A higher peak RG value is readily obtained with our design if only one radiation state is emphasized, as it was in those comparison systems. Second, the reconfigurable states of our design required the use of PIN diodes, inductors, and DC bias lines. They unavoidably led to a decrease of the overall radiation efficiency and, hence, peak RG values. Moreover, compared with the polarization-reconfigurable single-layer patch antenna in [26] that attains a ~ 6 dBi peak gain value with an electrical size, ka = 3.6, and an aperture area, 0.64 λ_0^2, our prototype achieved more than a 3 dBi value in all four states despite being 5.14 times electrically smaller and having an aperture area, 3.23 $\times 10^{-2}$ λ_0^2, that is twenty times smaller.

TABLE III
PERFORMANCE COMPARISON OF THE PROTOTYPE WITH RECENTLY REPORTED YAGI-CONFIGURED ESAS

Refs.	*ka*	Yagi Style*	FTBR (dB)	Real. Gain (dBi)	Num. of Elements	Reconfigurable
[12]	0.84	Ant-Director	10.2	8.8	2	No
[13]	0.75	Ant-Director	4.3	3.5	2	No
[14]	0.84	Ant-Director	5.4	5.0	2	No
[15]	0.97	Quasi	13.4	3.6	2	No
[16]	0.94	Ant-Reflector	23.2	6.2	2	No
[17]	0.94	Ant-Reflector	20.0	9.2	2	No
[18]	0.69	Ant-Reflector	11.4	3.6	2	No
Rep. Ant.	0.7	RDD	11, 11.1, 12.1, 11.2	3.1, 3.2, 3.0, 3.1	3	Yes

*Ant = antenna, RDD = Reflector-Driver-Director

IV. CONCLUSION

A Yagi-configured, NFRP-based polarization-reconfigurable ESA was presented. By controlling the ON/OFF states of four PIN diodes integrated into its driver element, the ESA achieved four polarization states, i.e., *x*-LP, *y*-LP, LHCP and RHCP. The simulated and measured results demonstrate impressive endfire performance for all four polarization states. The measured overlapping bandwidth between the –10-dB impedance bandwidth and 3-dB AR bandwidth for all four polarization states was 7 MHz, from 0.946 to 0.953 GHz. The demonstrated appealing performance characteristics of its electrically small design, including excellent directivity and FTBR values with quad-polarization diversity, make it attractive for the next-generation of narrowband wireless applications, e.g., WiFi, V2V and D2D connectivity, and RFID and wireless power transfer systems.

REFERENCES

[1] H. Yagi, "Beam transmission of ultra-short waves," *Proc. Inst. Radio Eng*., vol. 16, no. 6, pp. 715–740, Jun. 1928.

[2] Y. Mushiake, "A theoretical analysis of the multi-element end-fire array with particular reference to the Yagi-Uda antenna," *IRE Trans. Antennas Propag*., vol. 4, no. 3, pp. 441-444, Jul. 1956.

[3] Z. Hu, Z. Shen, W. Wu, and J. Lu, "Low-profile top-tat monopole Yagi antenna for end-fire radiation," *IEEE Trans. Antennas Propag*., vol. 63, no. 7, pp. 2851-2857, Jul. 2015.

[4] J. Huang and A. C. Densmore, "Microstrip Yagi array antenna for mobile satellite vehicle application," *IEEE Trans. Antennas Propag*., vol. 39, no. 7, pp. 1024–1030, Jul. 1991.

[5] H. Liu, S. Gao, and T. Loh, "Small director array for low-profile smart antennas achieving higher gain," *IEEE Trans. Antennas Propag*., vol. 61, no. 1, pp. 162-168, Jan. 2013.

[6] R. A. Alhalabi and G. M. Rebeiz, "High-gain Yagi-Uda antennas for millimeter-wave switched-beam systems," *IEEE Trans. Antennas Propag*., vol. 57, no. 11, pp. 3672-3676, Nov. 2009.

[7] R. A. Alhalabi and G. M. Rebeiz, "Differentially-fed millimeter-wave Yagi-Uda antennas with folded dipole feed," *IEEE Trans. Antennas Propag*., vol. 58, no. 3, pp. 966-969, Mar. 2010.

[8] Y. Cai, Y. J. Guo, and P. Qin, "Frequency switchable printed Yagi-Uda dipole sub-array for base station antennas," *IEEE Trans. Antennas Propag*., vol. 60, no. 3, pp. 1639-1642, Mar. 2012.

[9] M. Nasir, Y. Xia, M. Jiang, and Q. Zhu, "A novel integrated Yagi–Uda and dielectric rod antenna with low sidelobe level," *IEEE Trans. Antennas Propag*., vol. 67, no. 4, pp. 2751-2756, Apr 2019.

[10] G. R. DeJean, T. T. Thai, S. Nikolaou, and M. M. Tentzeris, "Design and analysis of microstrip bi-Yagi and quad-Yagi antenna arrays for WLAN applications," *IEEE Trans. Antennas Propag*., vol. 6, no. 2, pp. 244-248, Feb. 2007.

[11] T. Yang, D. Yang, and D. Geng, "Compact planar quasi-Yagi antenna with band-notched characteristic for WLAN and DSRC for ultra-wideband applications," *IET Microw. Antennas Propag.*, vol. 12, no. 7, pp. 1239-1245, Jun. 2018.

[12] S. Lim and H. Ling, "Design of electrically small Yagi antenna," *Electron. Lett.*, vol. 43, no. 5, pp. 3-4, Mar. 2007.

[13] J. J. Yu and S. Lim, "Design of an electrically small, circularly polarized, parasitic array antenna for an active 433.92-MHz RFID handheld reader," *IEEE Trans. Antennas Propag*., vol. 60, no. 5, pp. 2549-2554, May 2012.

[14] S. Lim, J. Chen, and C. Cato, "Design of a thin, electrically small, two-element parasitic array with circular polarization," *IEEE Antennas Wireless Propag. Lett.*, vol. 17, pp. 1006-1009, 2018.

[15] M.-C. Tang, B. Zhou, and R. W. Ziolkowski, "Flexible uniplanar electrically small directive antenna empowered by a modified CPW-feed," *IEEE Antennas Wireless Propag. Lett.*, vol. 15, pp. 914-917, 2016.

[16] M.-C. Tang and R. W. Ziolkowski, "Efficient, high directivity, large front-to-back-ratio, electrically small, near-field-resonant-parasitic antenna," *IEEE Access.*, vol. 1, pp. 16-28, 2013.

[17] M.-C. Tang and R. W. Ziolkowski, "Compact, two-element array with high broadside directivity," *IET Microw. Antennas Propag.*, vol. 7, no. 8, pp. 663-671, 2013.

[18] M.-C. Tang, R. W. Ziolkowski, S. Xiao, and M. Li, "A high-directivity, wideband, efficient, electrically small antenna system," *IEEE Trans. Antennas Propag*., vol. 62, no. 12, pp. 6541-6547, Dec. 2014.

[19] P. Qin, A. R. Weily, Y. J. Guo, and C. Liang, "Polarization reconfigurable U-slot patch antenna," *IEEE Trans. Antennas Propag*., vol. 58, no. 10, pp. 3383-3388, Oct. 2010.

[20] B. Li and Q. Xue, "Polarization-reconfigurable omnidirectional antenna combining dipole and loop radiators," *IEEE Antennas Wireless Propag. Lett.*, vol. 12, pp. 1102-1105, 2013.

[21] Y. Cai, S. Gao, Y. Yin, W. Li, and Q. Luo, "Compact-size low-profile wideband circularly polarized omnidirectional patch antenna with reconfigurable polarizations," *IEEE Trans. Antennas Propag*., vol. 64, no. 5, pp. 2016-2021, May. 2016.

[22] R. Chen and J. Row, "Single-fed microstrip patch antenna with switchable polarization," *IEEE Trans. Antennas Propag*., vol. 56, no. 4, pp. 922-926, Apr. 2008.

[23] Z. Yang, H. Yang, J. Hong, and Y. Li, "Bandwidth enhancement of a polarization-reconfigurable patch antenna with stair-slots on the ground," *IEEE Antennas Wireless Propag. Lett.*, vol. 13, pp. 579-582, 2014.

[24] Y. P. Selvam, L. Elumalai, M. G. N. Alsath, M. Kanagasabai, S. Subbaraj, and S. Kingsly, "Novel frequency- and pattern-reconfigurable rhombic patch antenna with switchable polarization," *IEEE Antennas Wireless Propag. Lett.*, vol. 16, pp. 1639-1642, 2017.

[25] Q. Chen, J. Li, G. Yang, B. Cao, and Z. Zhang, "A polarization-reconfigurable high-gain microstrip antenna," *IEEE Trans. Antennas Propag*., vol. 67, no. 5, pp. 3461-3466, May. 2019.

[26] B. Kim, B. Pan, S. Nikolaou, Y. Kim, J. Papapolymerou, and M. M. Tentzeris, "A novel single-feed circular microstrip antenna with reconfigurable polarization capability," *IEEE Trans. Antennas Propag*., vol. 56, no. 3, pp. 630-638, Mar. 2008.

[27] F. Farzami, S. Khaledian, B. Smida, and D. Erricolo, "Reconfigurable linear/circular polarization rectangular waveguide filtenna," *IEEE Trans. Antennas Propag*., vol. 66, no. 1, pp. 9-15, Jan. 2018.

[28] T. H. Gan, Z. Yang, E. L. Tan, J. X. Lim, M. Q. Huynh, and M. Mayank, "A polarization-reconfigurable filtering antenna system," *IEEE Antennas Propag. Magazine*, vol. 55, no. 6, pp. 198–219, Dec. 2013.

[29] L. Tan, R. Wu, and Y. Poo, "Magnetically reconfigurable SIW antenna with tunable frequencies and polarizations," *IEEE Trans. Antennas Propag*., vol. 63, no. 6, pp. 2772-2776, Jun. 2015.

[30] J. Hu, Z. Hao, and Z. Miao, "Design and implementation of a planar polarization-reconfigurable antenna," *IEEE Antennas Wireless Propag. Lett.*, vol. 16, pp. 1557-1560, 2017.

[31] E. E. Altshuler, T. H. O'Donnell, A. D. Yaghjian, and S. R. Best, "A monopole superdirective array," *IEEE Trans. Antennas Propag*., vol. 53, no. 8, pp. 2653–2661, Aug. 2005.

[32] MACOM. (2019). Products: BAR5002. [Online]. Available https://www.mouser.cn/datasheet/2/196/Infineon-BAR50SERIES-DS-v01_01-en-1225320.pdf

[33] MACOM. (2019). Products: LQW18ASR10G0ZD. [Online]. Available https://www.mouser.cn/datasheet/2/281/c51e-794816.pdf

[34] H. Arai and A. Noguchi, "A closely spaced switched beam antenna," in *Proc. International Workshop on Antenna Technologies (iWAT 2014)*, Sydney, Australia, Mar. 2014, pp. 166–167.

[35] StarLab Version D User Guide 1.0, Reference: TD. 224.1.08. SATF. A, SATIMO Corp., France, 2008.